Energy & Environmental Science

ROYAL SOCIETY OF CHEMISTRY

PAPER

View Article Online
View Journal | View Issue

Cite this: *Energy Environ. Sci.*, 2025, **18**, 8815

Direct visualization and mechanistic insights into initial lithium plating in anode-free lithium metal batteries

Jin Su *[ab] and Chun Huang *[abc]

Anode-free lithium metal batteries (AFBs), which use bare Cu current collectors, represent a promising energy storage technology that offers higher energy density than conventional lithium-ion batteries. Without a lithium metal anode, AFBs are easier to assemble and more cost-effective. However, they suffer from rapid capacity loss and short cycle life limiting their practical applications. A major challenge in their development lies in achieving an understanding of the cycling protocols and mechanisms needed to control the morphology and microstructure of the initial lithium anode growth on the Cu current collector (Cu-CC). In this study, we observed a significant pressure difference between the annular edge and center regions of the Cu-CC in coin cell type AFBs, which dramatically influenced the microstructural morphology of the initial lithium metal growth process. We demonstrated that lithium metal plated in the high-pressure annular edge region forms large, dense grains with a void-free internal structure and a smooth, flat surface, whereas in the low-pressure center region, lithium metal plating consists of small, loose, and tortuous grains with abundant voids and a rough surface. The pressure difference does not affect the solid electrolyte interphase (SEI) composition in these regions. This study provides a unified view on initial lithium metal plating on the bare Cu current collector in AFBs for achieving a uniform and dense lithium metal microstructure.

Received 9th April 2025,
Accepted 7th August 2025

DOI: 10.1039/d5ee01956g

rsc.li/ees

Broader context

It is challenging for lithium ion batteries with a graphite anode and lithium metal batteries with a lithium metal anode to further increase battery energy densities due to the bulky anodes. Anode-free lithium metal batteries completely eliminate the anode and have become a promising candidate because they further increase energy densities by 40–60%. However, anode-free batteries suffer from relatively shorter cycle life due to heterogeneous lithium plating and uncontrollable growth of lithium structures. Here, we combine chemical composition characterisation and morphology observation techniques, and reveal that the root cause of the heterogeneous lithium structure growth is due to the uneven pressure exerted inside the batteries. This study provides fundamental understanding of the lithium structure growth mechanisms for achieving more uniform lithium plating and longer cycling life of new anode-free batteries.

Introduction

Lithium metal, with its high theoretical specific capacity of 3860 mA h g^{-1}, volumetric capacity of 2046 mA h cm^{-3}, and lowest redox potential (−3.04 V_{SHE}), enables lithium metal batteries (LMBs) to achieve significantly higher energy density and voltage compared to conventional lithium-ion batteries.[1–7] Anode-free lithium metal batteries (AFBs), which utilize bare Cu as the anode current collector without requiring a lithium metal anode, offer higher energy density, simplify manufacturing processes, reduce costs, and hold significant promise for applications in electric vehicles and intermittent renewable solar energy storage.[8–16] AFBs rely on lithium released from the cathode material, the sole lithium source, during the first charge to form lithium metal plating on the Cu current collector (Cu-CC).[8–11] However, the lithium inventory gradually depletes, leading to rapid capacity fading compared to lithium metal batteries with excess lithium in the anode.[17–19] The primary factor contributing to the poor cycling stability of AFBs is the irreversible consumption of the lithium inventory.[17–23]

Many research efforts have been made to optimize both the current collectors and electrolytes of AFBs to enhance lithium

[a] *Department of Materials, Royal School of Mines, Imperial College London, London SW7 2AZ, UK. E-mail: sujin23@outlook.com, a.huang@imperial.ac.uk*
[b] *The Faraday Institution, Quad One, Harwell Science and Innovation Campus, Didcot OX11 0RA, UK*
[c] *Research Complex at Harwell, Rutherford Appleton Laboratory, Didcot, OX11 0FA, UK*

plating and stripping uniformity, thereby prolonging their cycle life.[24–30] Surface modification on the Cu-CC, use of locally high-concentration electrolytes, and optimization of the first-cycle protocol can improve the uniformity and morphology of lithium plating. For improving the cycling performance of AFBs, the most critical stage is the initial formation of the lithium metal anode. A favourable initial lithium metal formation process significantly enhances the subsequent cycling performance of AFBs.[8–10] The redox shuttle mechanism for reactivating dead lithium and the design of dynamically lithium-compensated polymer-based artificial SEIs provide valuable perspectives for improving lithium utilization efficiency and cycling stability.[31,32] However, there is still a lack of understanding of the optimal cycling protocols and mechanisms for controlling the morphology and microstructure of the initial lithium metal growth. Although some research groups have explored the effects of pressure on LMBs, attempting to understand the growth of lithium metal, most of these studies are focused on Peek Swagelok cells and solid-state batteries.[33–36]

Coin cell type batteries are the most widely used configuration for studying AFBs. Some studies have examined the influence of stack pressure on the cycling performance of coin cell LMBs.[37,38] However, the effects of pressure distribution and uniformity within coin cell type AFBs on the growth and microstructure of initial lithium metal plating remain insufficiently explored. A better understanding of the internal pressure distribution effects in coin cell type AFBs will not only provide deeper insights into the key factors influencing the initial lithium metal plating but also contribute to establishing a unified and comparable reference. To accurately analyse the distribution and microstructure of initial lithium metal plating locations on the Cu-CC surface, it is crucial to qualitatively detect lithium with high sensitivity and to visualize lithium microscopic spatial distribution. Time-of-flight secondary ion mass spectrometry (ToF-SIMS) offers significant advantages for detecting lithium metal, including high sensitivity, 2D imaging, and 3D depth profiling. The ToF-SIMS mapping technique provides detailed information on the spatial distribution of lithium metal. However, energy-dispersive X-ray spectroscopy (EDX) cannot detect lithium metal.[39,40]

In this study, using ToF-SIMS and plasma FIB-SEM imaging, we demonstrated the microstructure morphology of lithium metal growth on the Cu-CC in AFBs and identified the key factors that influence initial lithium plating uniformity and morphology. Through internal pressure distribution tests of coin cell type AFBs, we observed a significant pressure distribution difference on the Cu-CC surface: the annular edge region experienced a much higher pressure (50 MPa) than the central region ($\sim$1 MPa), resulting in distinct microstructural differences in the initial lithium metal plating. The high-pressure annular edge region exhibited lithium metal with a dense, void-free internal structure and a smooth, flat surface, whereas the low-pressure center region resulted in lithium metal with loose, tortuous grains, abundant voids, and a rough surface. Furthermore, adjusting the assembly pressure of the coin cell type AFBs did not mitigate this pressure distribution difference or the resulting microstructural variations in initial lithium metal plating. However, the pressure distribution difference did not alter the SEI layer composition in the two regions. This study provides a unified view on the initial lithium metal growth process on the Cu-CC and provides a strategy for achieving a uniform and favorable lithium metal microstructure in AFBs.

Results and discussion

To study the microstructure and uniformity of the initial lithium metal plating on the Cu current collector, a galvanostatic lithium plating at 0.05 mA cm^{-2} was applied to the Li||Cu cells, with the corresponding potential profile shown in Fig. 1(a). Throughout the 100 h initial lithium plating on the Cu-CC, the potential remained highly stable. The magnified potential profiles are shown in the inset of Fig. 1(a). During the beginning of 0.1 h lithium plating, the open-circuit potential of 1.9 V significantly declined due to the nucleation of lithium metal on the Cu-CC surface and SEI formation, ultimately reaching a nucleation potential of -71 mV. After lithium nucleation and SEI formation, the polarization potential started reducing, marking the start of stable lithium plating on the surface of the Cu-CC. As the lithium plating capacity increased, the polarization potential remained stable at -7.0 mV after 25 h (capacity of 1.25 mA h cm^{-2}), 50 h (2.5 mA h cm^{-2}) and 100 h (5 mA h cm^{-2}), as shown in Fig. 1(a), indicating that the interface reaction was stable throughout the entire lithium plating process.

The images in Fig. 1(b)–(e) show the states of initial lithium metal plating at gradually increasing capacities on the Cu-CC surface. Fig. 1(b) presents the originally smooth, bare Cu-CC surface. After plating lithium metal at a capacity of 1.25 mA h cm^{-2} (Fig. 1(c)), the Cu surface displayed randomly distributed small greyish-black spots. When the capacity was increased to 2.5 mA h cm^{-2} (as shown in Fig. 1(d)), a significant denser and thicker lithium metal layer was plated in the annular edge region, while the central region retained a dark-spot feature. When the capacity reached 5 mA h cm^{-2}, a dense lithium metal layer covered the entire Cu-CC surface, as shown in Fig. 1(e). The internal pressure distribution of the coin cell type AFBs was tested, with a structural diagram shown in Fig. 1(f). Different assembly pressures (0.6, 0.7, 0.8, 0.9, and 1.0 tons) were used to examine how varying pressures impact the internal pressure distribution in the coin cell type AFBs, as shown in Fig. 1(k) and Fig. S1. At 0.6 tons, pressure is concentrated in a narrow annular edge region with highly uneven distribution (Fig. S1b). At 0.7 tons, the width of the high-pressure annular edge region increases, but the pressure distribution remains non-uniform (Fig. S1c). Since coin cells typically use stainless-steel spacers and annular springs, both of which are high in hardness, they create an annular shaped pressure distribution on the Cu-CC, as illustrated in Fig. 1(i) and 1(g).

When the assembly pressure increased to 0.8 tons, the pressure distribution improved significantly, with a larger annular edge region experiencing pressure above 50 MPa, although parts of the central region still received $\sim$1 MPa pressure, as shown in Fig. S1d. At 0.9 and 1.0 tons, the edge region with high pressure expands only slightly, but becomes more asymmetric

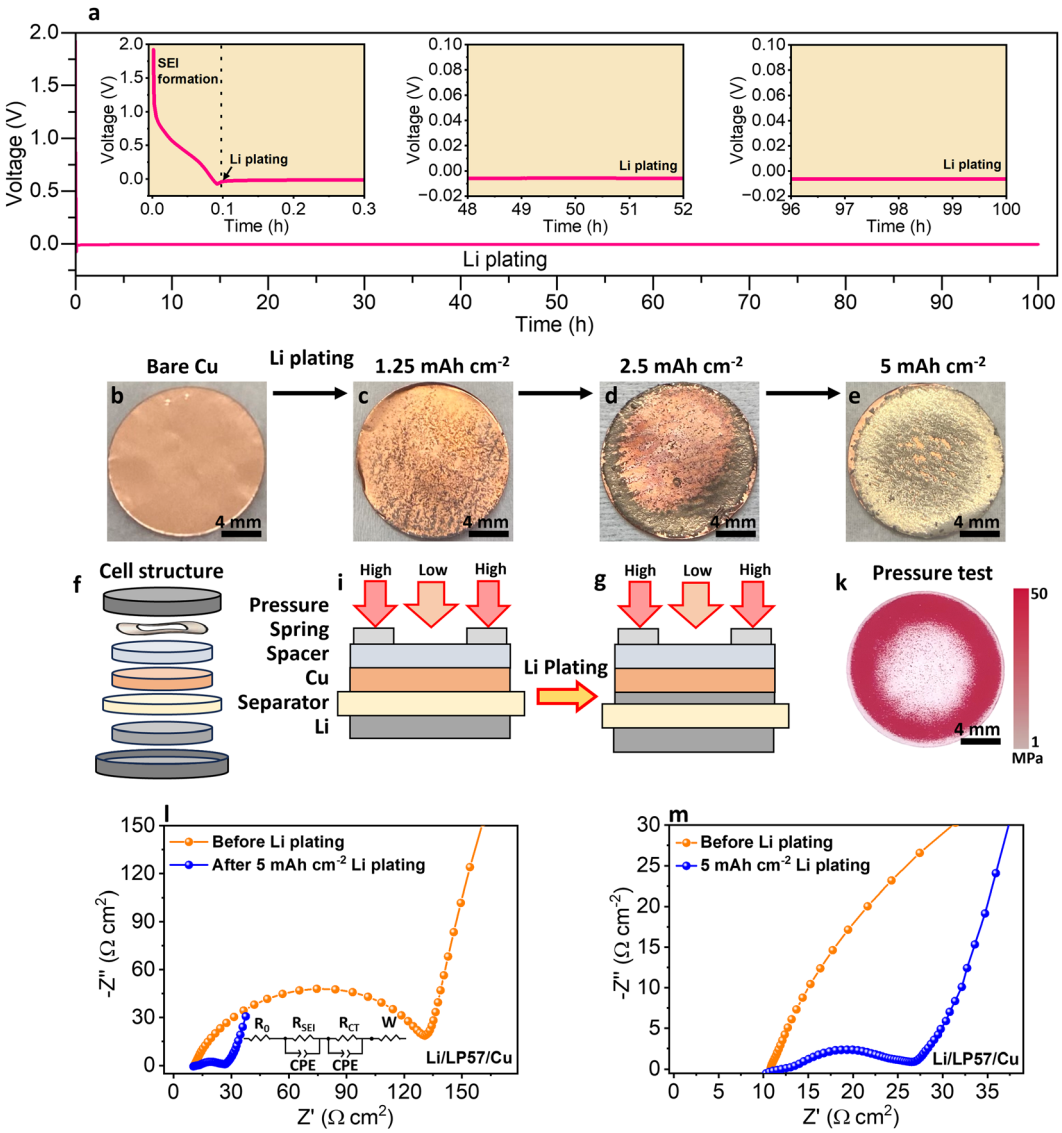

Fig. 1 (a) Potential response of the Li||Cu cell for initial lithium plating on a Cu-CC at a current density of 0.05 mA cm^{-2}. (b)–(e) Photographs of the initial lithium metal plated on the Cu-CC at different capacities. (f) Schematic illustration of the internal structure of the Li||Cu coin cell, and the internal pressure distribution of the coin cell before (i) and after (g) lithium metal plating. (k) Pressure distribution measurement on the Cu-CC surface in the coin cell type AFBs. (l) EIS plots of the Li||Cu coin cells before and after 5 mA h cm^{-2} of initial lithium plating, along with (m) magnified EIS plots.

and uneven (Fig. S1e and f), and no further improvement in uniformity is observed. Ensuring uniform pressure distribution within the AFBs across all directions and maintaining even pressure on the Cu-CC surfaces are essential for achieving uniform lithium metal plating. In addition, the repeated pressure distribution test was also conducted under 0.8 tons conditions (Fig. S1g), which confirmed high reproducibility of the annular pressure profile. Therefore, 0.8 tons is the optimal pressure for achieving relatively uniform pressure distribution and reproducible lithium deposition morphology in coin cell type AFBs. In this study, we use the optimal assembly pressure of 0.8 tons to prepare coin cell AFBs for lithium metal plating research. It is essential to emphasize that this pressure distribution testing result provides solid evidence that the annular shaped pressure distribution within the coin cell directly influences the overall morphology of initial lithium plating on Cu-CC in AFBs. We have compared different configurations under the same coin cell assembly pressure of 0.8 tons: (a) the standard wave-type spring, (b) a conical-type spring, and (c) two stainless steel spacers instead of spring. The results confirm that changing the spring type or replacing it with rigid spacers alters the internal pressure profile but does not eliminate the inherent non-uniformity of pressure distribution within coin cell type AFBs. Among the tested configurations, the wave-type spring provides the most uniform and reproducible annular pressure profile, making it the most suitable option for isolating and studying the effects of pressure distribution on lithium metal plating behavior. We implemented careful alignment and calibration of each cell during assembly, as illustrated in Fig. S2, ensuring a consistent internal configuration across all samples. The lithium plating

was well-confined to the Cu-CC surface, with no observable side deposition on unintended internal components (Fig. S3). We used the low current density to ensure stable and uniform lithium deposition throughout the entire process and investigated higher current densities of up to 0.5–1.0 mA cm^{-2} (Fig. S4).

Due to the pressure distribution difference between the annular edge and central regions of the Cu-CC, and the softness of lithium metal, which deforms easily under pressure,[41] 5 mA h cm^{-2} of lithium plated in the high-pressure annular edge regions was compressed into a smoother surface, forming a bright silver ring shape around the annular edge in Fig. 1(e). Meanwhile, the lower pressure central region resulted in a rougher lithium surface, increasing light scattering and giving it a darker gray appearance. At a lithium plating capacity of 2.5 mA h cm^{-2}, lithium metal in the low-pressure central region grew as randomly distributed small protrusions. In contrast, lithium deposited in the high-pressure annular edge region experienced significantly greater compression, resulting in a denser bulk and smoother surface. The combined influence of high pressure and the lower overpotential for lithium plating on a Li metal surface (−11 mV), compared to the high reduction overpotential (−71 mV) for lithium deposition on the Cu-CC surface (as shown in Fig. S5), these factors collectively contributed to the observed lithium plating behavior. Consequently, lithium preferentially plated on the lithium surface, leading to increased lithium deposition in the annular edge region, as illustrated in Fig. 1(d).

Additionally, electrochemical impedance spectroscopy (EIS) testing was conducted on the Li||Cu cell to measure the initial resistance and post-deposition impedance after initial lithium plating with a capacity of 5 mA h cm^{-2}, as shown in Fig. 1(l)–(m). At high frequencies, R_0 representing electrolyte resistance remained at 10 Ω cm^{-2}, indicating that no side reactions occurred in the electrolyte and separator after 5 mA h cm^{-2} lithium metal plating. After 5 mA h cm^{-2} lithium plating, the SEI layer resistance (R_{SEI}) and charge transfer resistance (R_{CT}) clearly decreased (Table S1) at the anode interface, demonstrating that the SEI layer formed after initial lithium plating on the Cu-CC enhanced lithium-ion transport compared to the intrinsic oxide layer on the Cu-CC. The plated lithium under low current density promotes the formation of a more compact and conductive interface, facilitating improved electrochemical kinetics. Specifically, the large decrease in R_{CT} (from 113.4 to 12.0 Ω cm^2) indicates a more uniform and dense lithium morphology, enhancing charge transfer processes.

To investigate the composition, crystallinity, and phase purity of the plated lithium metal, X-ray photoelectron spectroscopy (XPS) and X-ray diffraction (XRD) were used to analyze the lithium plated Cu-CC. XPS analysis was conducted on the annular edge region of the Cu-CC with 5 mA h cm^{-2} of initial lithium metal plating as well as on the surface of the bare Cu current collector, as shown in Fig. 2(a). In the blue XPS survey spectrum for the bare Cu, only Cu, O, and C excitation peaks were prominent, indicating the presence of intrinsic copper oxide on the Cu-CC surface. After plating 5 mA h cm^{-2} of lithium metal on the Cu-CC, the orange XPS survey spectrum showed F 1s, P 2p, and Li 1s excitation peaks at 687, 134, and 55 eV, respectively, while the Cu signal had disappeared, and the O 1s and C 1s peaks were significantly attenuated. This indicates that lithium metal had been deposited on the Cu-CC surface, with an SEI layer composed of Li, O, F, and P elements present on the lithium surface. Additionally, XRD patterns of the annular edge region of the Cu-CC with 5 mA h cm^{-2} of lithium deposition and the bare Cu-CC were analyzed, as shown in Fig. 2(b). The XRD peaks of the bare Cu-CC only showed signals at 43.7° and 50.7°, corresponding to the Cu (111) and Cu (200) crystal orientations. In contrast, after plating 5 mA h cm^{-2} of lithium metal on the Cu-CC, a Li (110) diffraction peak appeared at 36.4°, and an additional diffraction peak attributed to LiF (or Li_2CO_3) from the SEI layer was observed at 42.4°.

XRD patterns of plated lithium metal with 10 mA h cm^{-2} capacity and a pristine lithium metal chip were also analyzed, as shown in Fig. 2(c) and (d) (magnified). For 10 mA h cm^{-2} capacity lithium plating, the plated lithium entirely covered the surface of the Cu current collector, and the edge region remained a silver-white annular shape, and the central region was grey, as depicted in Fig. S6. In the XRD pattern of the pristine lithium metal chip, three strong lithium metal diffraction peaks can be clearly observed at 36.4°, 52.4°, and 65.4°, corresponding to Li (110), Li (200), and Li (211), respectively. Additionally, diffraction peaks at 33.1°, 42.4°, and 49.7° were associated with Li_2CO_3, LiF (or Li_2CO), and LiOH, respectively. It is evident that with an increasing capacity of lithium metal plating (thus an increase in lithium metal thickness) the intensity of the Li (110) diffraction peak at 36.4° significantly increased and Li (220) diffraction increased slightly (as shown in Fig. S7), while the diffraction peaks of Li_2CO_3, LiF, and LiOH at 42.4° and 49.7° also showed a slight increase in intensity, indicating the surface SEI layer. When comparing the smaller capacity of lithium metal plating (2.5 mA h cm^{-2}), there was no lithium metal signal at 36.4°, due to the thin lithium metal layer having smaller grains and lower crystallinity, as shown in Fig. 2(e) and Fig. S7a and its magnified section in Fig. 2(f) and Fig. S7b.

To understand the microscopic morphology of initial lithium metal plating on the Cu current collector, top-view and PFIB cross-sectional SEM images were obtained from the annular edge and center regions of the Cu-CC with varying plating capacities, as shown in Fig. 3(a)–(l) and 4(a)–(l). A cryogenic environment was employed during plasma FIB cross-sectioning to minimize beam damage to lithium metal. ToF-SIMS depth profiling (Fig. 3(m)) further confirmed that the Cu-CC consists solely of Cu from the surface to the bulk. After plating 1.25 mA h cm^{-2} of lithium metal on the Cu-CC, the surface morphology of the annular edge region (Fig. 3(b)) showed micron-sized lithium grains forming lithium metal layers larger than 40 μm in size. The PFIB cross-sectional SEM image (Fig. 4(b)) showed that these lithium layers were ~5 μm thick with internal voids. In the center region (as shown in Fig. 3(f) and (j)), micron-scale granular lithium metal was observed, with PFIB cross-sectional images showing that these small lithium grains were less than 1 μm thick (Fig. 4(f) and (j)). When the capacity was increased to 2.5 mA h cm^{-2}, the Cu-CC surface in the annular edge region was covered by tortuous

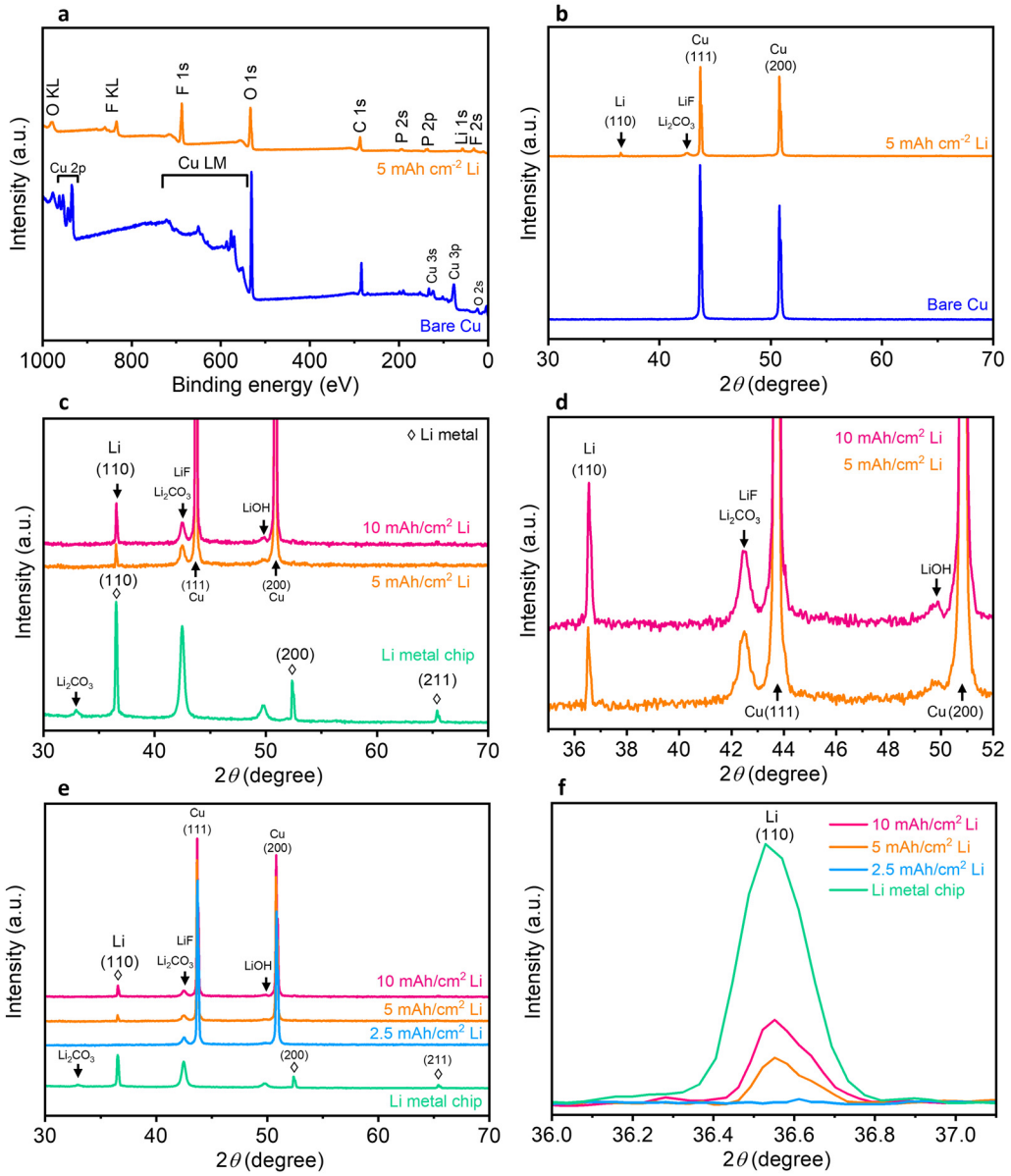

Fig. 2 (a) XPS survey spectra and (b) XRD patterns of the 5 mA h cm^{-2} plated initial lithium and bare Cu-CC. (c) XRD patterns of a lithium metal chip, 5 and 10 mA h cm^{-2} lithium metal plating, along with their magnified patterns (d). (e) XRD patterns of a lithium metal chip, 2.5, 5, and 10 mA h cm^{-2} lithium metal plating, as well as their magnified Li (110) peak patterns (f).

lithium metal grains exceeding 20 μm in size, with numerous grain boundaries and voids (as shown in Fig. 3(c)). PFIB cross-sectional SEM images (Fig. 4(c)) revealed that the tens of micron scale lithium metal grains were tortuous and intertwined with abundant voids and grain boundaries, closely resembling surface morphology. In the center region (as shown in Fig. 3(g) and (k)), the lithium metal showed micro sized grains forming tens of micron scale layers. The corresponding PFIB cross-sectional SEM images (Fig. 4(g) and (k)) clearly showed that these lithium layers were elevated in the middle and lower at the edges, with thicknesses ranging from 2 to 5 μm, containing numerous voids and grain boundaries.

When the capacity was further increased to 5 mA h cm^{-2}, top-view SEM images (Fig. 3(d)) showed that the annular edge region was fully covered with dense and large lithium grains. Most grains exceeded 20 μm in size. PFIB cross-sectional SEM images (Fig. 4(d)) demonstrated that voids within the lithium metal at the annular edge region disappeared entirely, with the lithium grains becoming dense and smooth-edged. The lithium grains also showed significant volumetric growth, exceeding 29 μm in size. The dense microstructure morphology of large lithium grains in the annular edge region was attributed to the compression exerted by the high pressure of 50 MPa (as shown in Fig. 1(k)). In the center region, the lithium microstructure morphology remained slender and tortuous, with abundant grain boundaries and voids (Fig. 3(h) and (l)). The corresponding PFIB cross-sectional SEM images (Fig. 4(h) and (l)) also showed that the lithium metal contained numerous grain

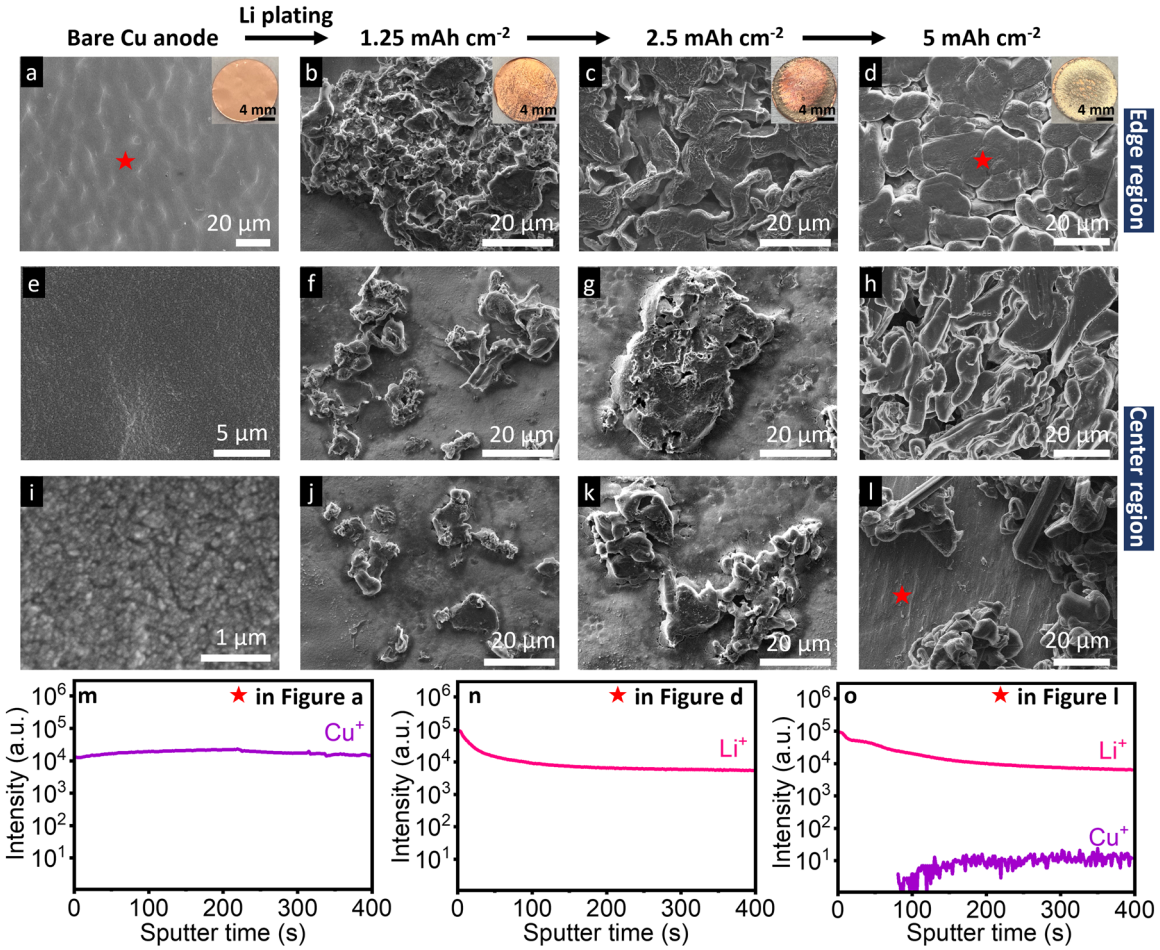

Fig. 3 (a)–(l) Top-view SEM images of the bare Cu-CC surface at different scales and annular edge and center regions of lithium metal plating with various capacities. (m)–(o) ToF-SIMS depth profiles of specific regions ★ (a, d, and l).

boundaries and voids. Surface morphology was imaged without Pt coating, and cross-sectional morphology was protected by a carefully deposited Pt layer under low ion current to preserve the lithium morphology underneath and minimize any ion beam milling-induced damage.

The dense microstructure morphology of lithium metal in the annular edge region and the loose morphology in the center region reflect the pressure distribution test results (as shown in Fig. 1(k)). The dense lithium metal layer in the annular edge region showed a thickness of 23 μm, while the loose lithium metal layer in the center region measured 28 μm (as shown in Fig. 4(d) and (f)). PFIB cross-sectional SEM continuous slicing images from the annular edge and center regions (Fig. S8) showed that the dense internal microstructure morphology in the annular edge region and the loose internal morphology in the center region were consistent throughout their respective entire 3D internal microstructure morphology. ToF-SIMS depth profiling in Fig. 3(n) revealed that the annular edge region, from the surface to the interior of the lithium metal layer, showed only lithium-ion signals. The area in the center region (★ in Fig. 3(l)) that appeared uncovered by lithium metal was not bare Cu-CC surfaces. As shown in Fig. 3(o), which was covered by a thin layer of lithium metal, at least 8 nm thick, as Cu ion signals only appeared after ion sputtering for 100 s.

To investigate the spatial distribution and composition for lithium plating, ToF-SIMS mapping was performed on the annular edge and center regions at different lithium plating stages, as shown in Fig. 5 and 6. The ion mapping images of the bare Cu surface (Fig. 5(a), (e) and 6(a), (e)), along with optical and total ion images at different scales (Fig. 5(i), (m) and 6(i), (m)), indicate that the smooth and flat Cu-CC surface exhibited some textures and undulations in its microscopic structure. The uniform distribution of Cu^+ and O^+ ions on the Cu-CC surface suggests that the intrinsic copper oxide layer was evenly distributed. When 1.25 mA h cm^{-2} capacity of lithium metal was plated on the Cu-CC surface, the optical and ion images of the annular edge and center regions were recorded (Fig. 5(i), (n) and 6(i), (n)), which reveal that the thick lithium metal did not uniformly cover the Cu-CC surface. However, the very weak Cu^+ ion mapping signals across the entire area (Fig. 5(b) and 6(b)) and the strong lithium-ion mapping signals (Fig. 5(f) and 6(f)) indicated that the plated lithium metal had already covered the entire Cu-CC surface.

When the lithium plating capacity was increased to 2.5 mA h cm^{-2}, the optical and total ion images of the annular edge

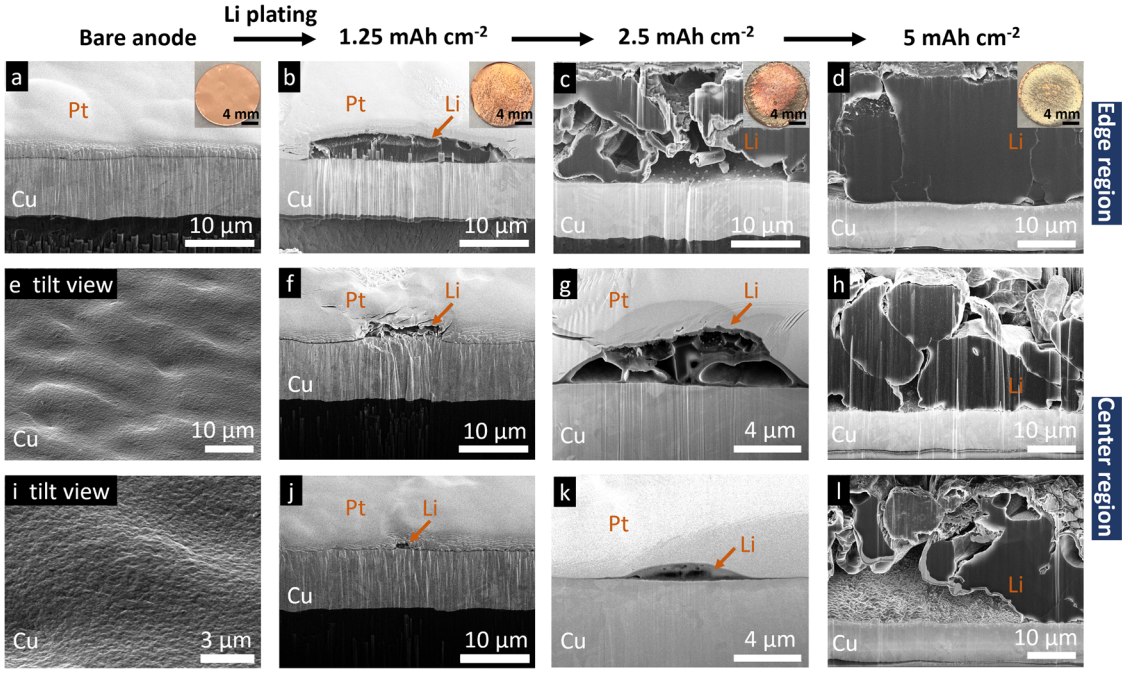

Fig. 4 (a)–(l) PFIB cross-section SEM images of the bare Cu-CC surface at different scales and the annular edge and center regions of various capacities lithium metal plating.

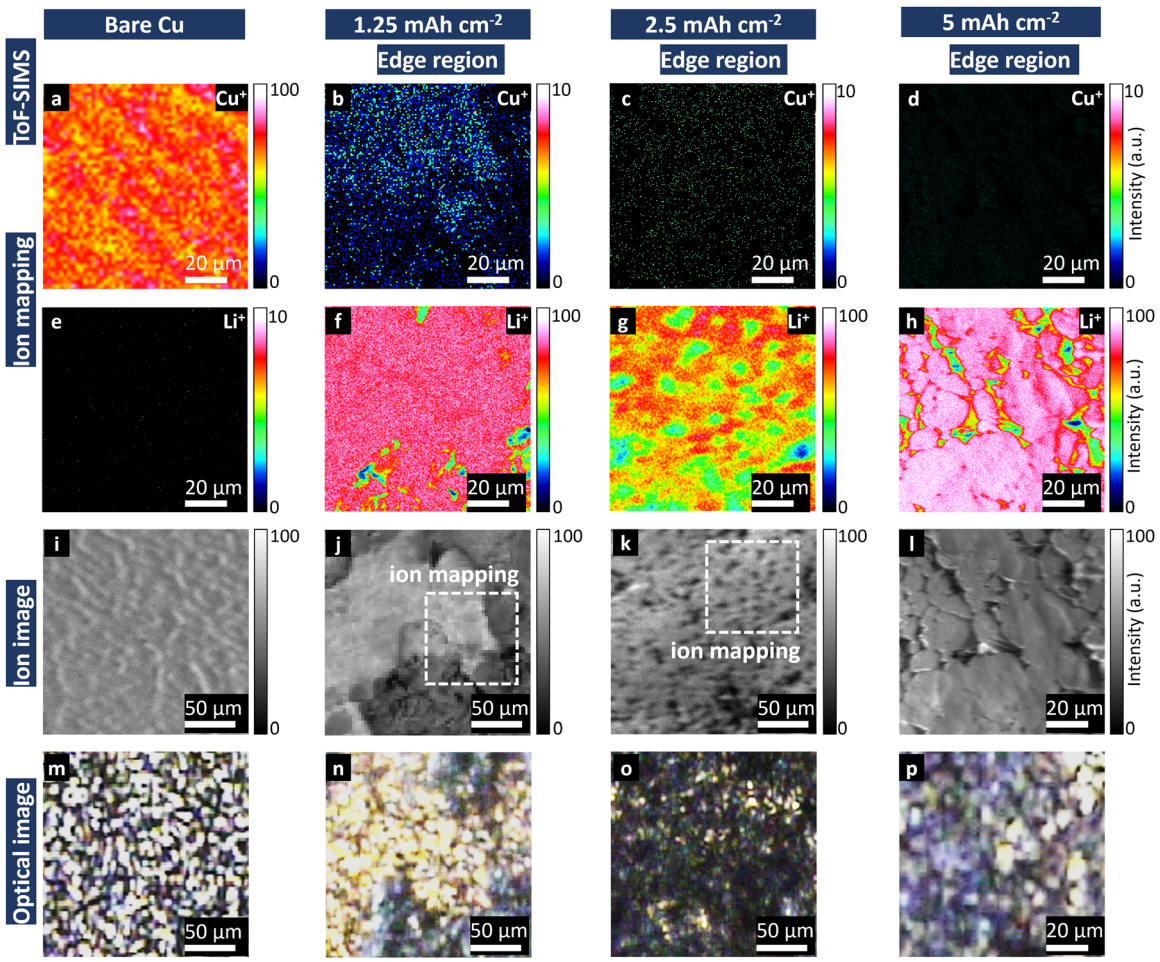

Fig. 5 (a)–(l) ToF-SIMS mapping and (m)–(p) optical images of the bare Cu-CC surface and annular edge regions of lithium metal plating with various capacities. The specific regions of Cu^+ and Li^+ ion mapping were marked within the larger-scale total ion images (j) and (k).

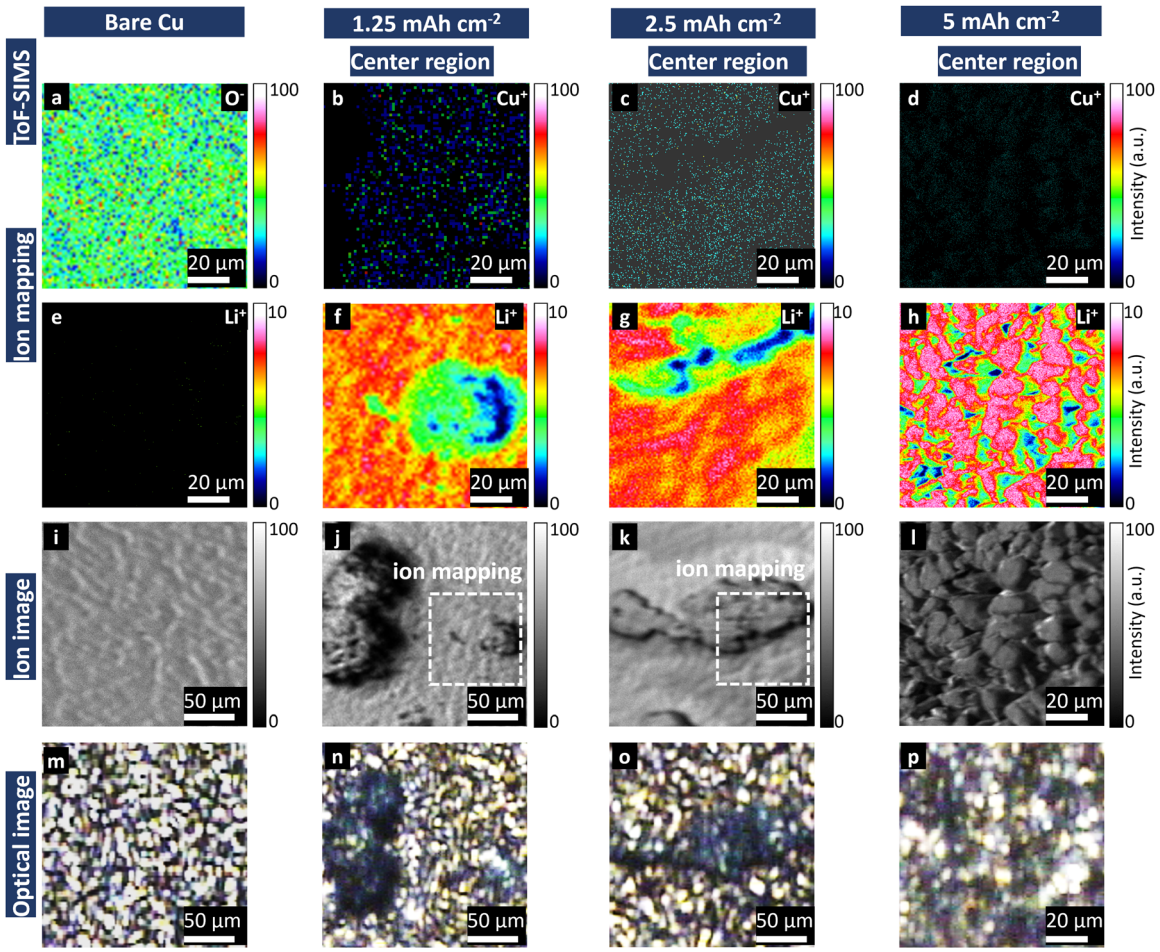

Fig. 6 (a)–(l) ToF-SIMS mapping and (m)–(p) optical images of the bare Cu-CC surface and center regions of various capacities lithium metal plating. The specific regions of Cu^+ and Li^+ ion mapping were marked within the larger-scale total ion images (j), (k).

region (Fig. 5(k) and (o)) showed that the thicker lithium metal layer fully covered the Cu-CC. The Cu^+ ion mapping signal (Fig. 5(c)) disappeared entirely, while the lithium-ion mapping signal (Fig. 5(g)) remained strong throughout the area, confirming that the dense lithium metal layer had completely covered the Cu-CC surface. The Li^+ ion mapping signal (Fig. 6(g)) remained strong across the entire region, while the Cu^+ ion mapping signal (Fig. 6(c)) was very weak, confirming that the plated lithium metal had entirely covered the Cu-CC surface.

Finally, when the lithium plating capacity was increased to 5 mA h cm^{-2}, the optical and total ion images of the annular edge region (Fig. 5(p) and (l)) showed a significant increase in

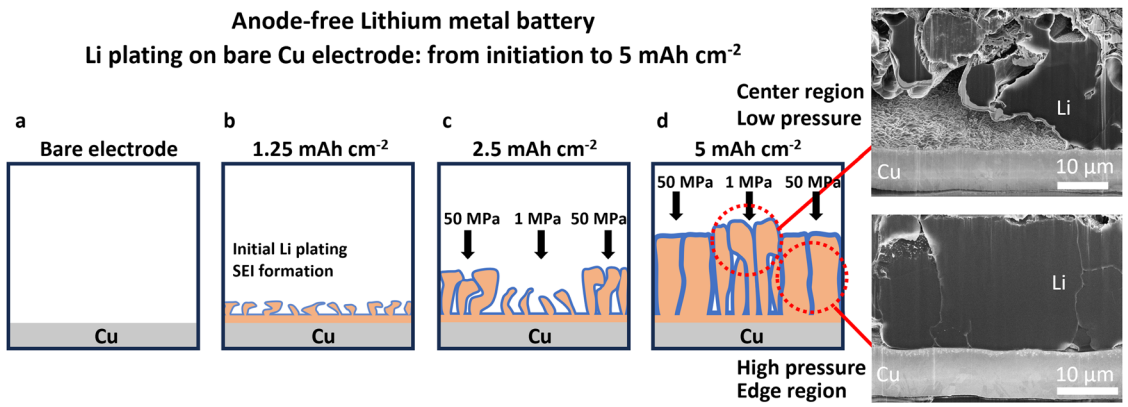

Fig. 7 (a)–(d) Schematic illustration of the initial lithium metal plating process on the Cu-CC surface in coin cell type AFBs.

the size of lithium metal grains. The Cu^+ ion mapping (Fig. 5(d)) showed no signal, while the Li^+ ion mapping (Fig. 5(h)) exhibited a very strong bright pink signal, indicating fully covering by dense lithium metal. Moreover, this region was densely filled with large lithium grains measuring 20–40 μm in size, consistent with the SEM images (as shown in Fig. 3(d)). In contrast, at this stage, the optical and ion images of the center region (Fig. 6(l) and (p)) revealed smaller lithium metal grains. The Cu^+ ion mapping (Fig. 6(d)) showed no signal, indicating that the Cu-CC was entirely covered by plated lithium metal. The Li^+ ion mapping (Fig. 6(h)) further confirmed that the lithium metal grains in the center region range from 10 to 20 μm in size. These green areas in Fig. 6(h) indicated fewer Li^+ ions per unit area, which corresponded to the voids and grain boundaries between the lithium metal grains, consistent with the SEM images (as shown in Fig. 3(h)). Through ToF-SIMS Li^+ and Cu^+ ion mapping, the surface morphology and spatial distribution of initial lithium metal plating were precisely analyzed, confirming the distinct microstructures of lithium plating in the annular edge and center regions on the Cu-CC surface in coin cell AFBs, which aligns with the internal pressure distribution testing in coin cell AFBs (as shown in Fig. 1(k)).

Based on the observed surface and internal microstructure morphologies, along with Li^+ mapping analysis in the annular edge and center regions of lithium metal plating on Cu-CC, we propose an initial lithium plating mechanism in coin cell AFBs, as illustrated in Fig. 7: at the initial stage, as lithium plating capacity increases to 1.25 mA h cm^{-2} (as shown in Fig. 7(b)), the randomly distributed lithium protrusions on the Cu-CC surface (Fig. 7(a)) grow to the micron scale (as shown in Fig. 3(f)). When the lithium plating capacity reaches 2.5 mA h cm^{-2}, the plated lithium metal was compressed by the higher pressure in the annular edge region, resulting in a smoother surface and denser microstructure (Fig. 7(c)). Furthermore, due to the smaller overpotential for lithium plating on Li metal surfaces, most lithium preferentially deposits in the annular edge region forming an annular shaped lithium metal layer (as shown in Fig. 1(d)). As the lithium plating capacity increases to 5 mA h cm^{-2} (Fig. 7(d)), the annular edge region, subjected to a pressure of 50 MPa, forms a highly compact lithium metal layer composed of large, dense grains with no internal voids (Fig. 3(d), 4(d) and 5(h)). In contrast, the center region, under much lower pressure (~1 MPa), forms a more porous and loosely packed lithium layer, consisting of small and tortuous grains with numerous

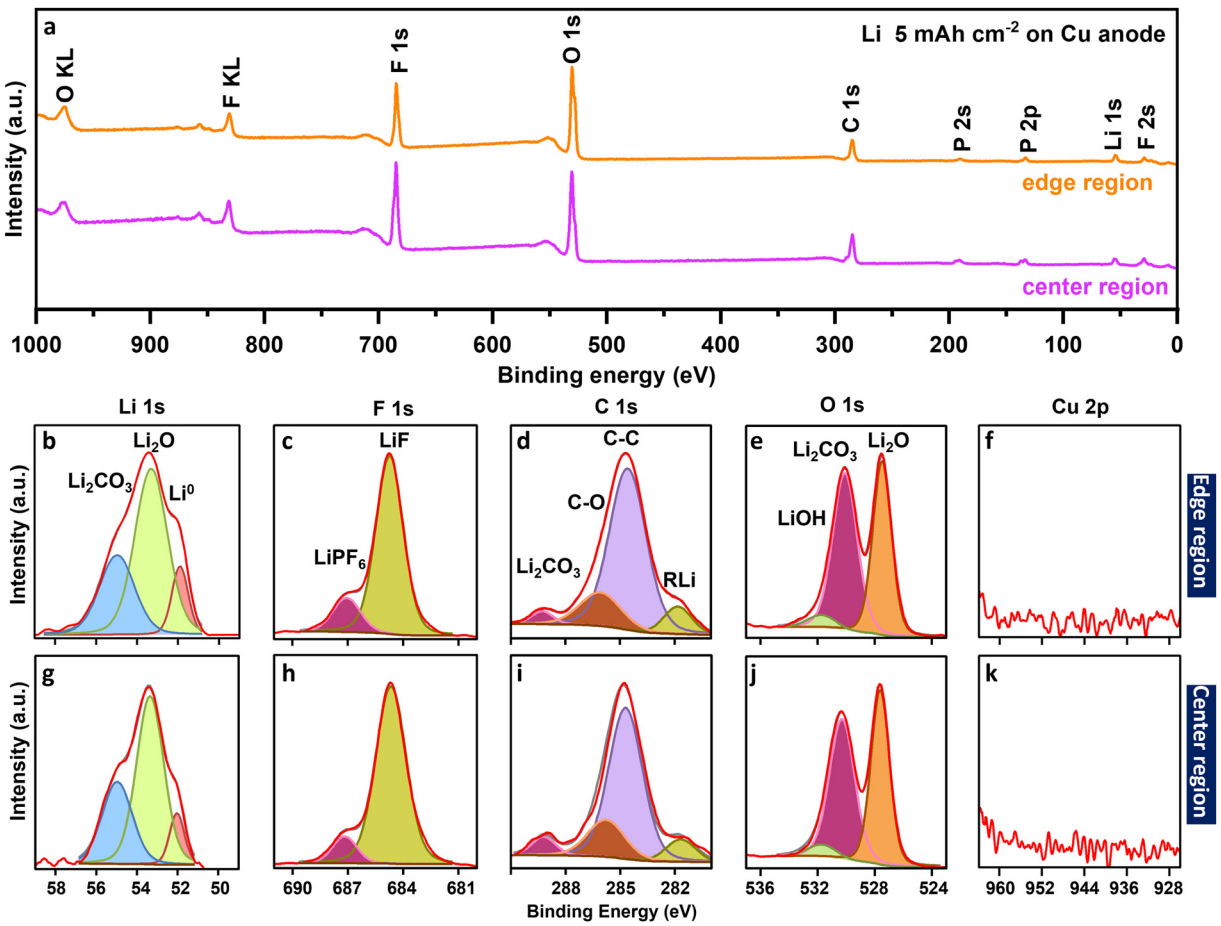

Fig. 8 (a) XPS survey spectra of the annular edge and center regions in plated lithium metal at a capacity of 5 mA h cm^{-2}. High-resolution XPS spectra of the (b)–(f) annular edge and (g)–(k) center regions in 5 mA h cm^{-2} plated lithium metal, showing Li 1s, F 1s, C 1s, O 1s, and Cu 2p excitation peaks.

grain boundaries and voids (as shown in Fig. 3(h), 4(h) and 6(h)). The dense lithium metal layer in the annular edge region (23 μm thick) was clearly thinner than the loosely packed lithium layer in the center region (28 μm).

To analyze the surface composition of the annular edge and center regions of plated lithium metal at a capacity of 5 mA h cm^{-2}, XPS analysis was conducted, as shown in Fig. 8. The XPS survey spectra (Fig. 8(a)) revealed that the surface of both the annular edge and center regions exhibited Li 1s, P 2p, and F 1s excitation peaks at 54 eV, 133 eV, and 685 eV, respectively. All the peak intensities in these two regions were similar, indicating that both regions had similar surface compositions and SEI components. The absence of Cu excitation peaks in both survey spectra further confirmed that lithium metal had completely covered the Cu-CC surface. To provide a more detailed analysis of the SEI layer, high-resolution XPS scans and corresponding peak fitting were performed as shown in Fig. 8(b)–(k). The excitation peaks at 54 eV, 285 eV, 528 eV, and 952 eV corresponding to Li 1s, F 1s, C 1s, O 1s, and Cu 2p, along with peak fitting analysis revealed that the surface compositions of the two regions were highly similar, which was likely due to the identical electrolyte in contact with both regions. Despite the significant difference in the pressures that were subjected by the two regions, the pressure variation did not appear to affect the SEI layer composition on the surface on initial lithium metal plating. XPS peak fitting analysis revealed that the SEI layer in both regions primarily consisted of Li_2CO_3, LiF, and LiOH, consistent with XRD results (Fig. 2(e)).

It is important to note that, for stable and efficient cycling performance of AFBs, the initially plated lithium metal layer should process a dense and uniform microstructure. This work demonstrated that the microstructure morphology of the initially plated lithium metal with a capacity of 5 mA h cm^{-2} in the annular edge region of the coin cell exhibits large lithium grains, a smooth surface, and a dense, uniform, void-free internal microstructure. The plated lithium metal in the center region did not meet these criteria due to its small, loosely packed grains with abundant voids and a rough surface. The root cause of this disparity is that the edge region experiences significantly higher pressure than the center region. Although adjusting the assembly pressure of the coin cell does not improve the uniformity of the pressure distribution on the Cu-CC surface, further investigation is needed to modify the internal configuration of coin cell AFBs to achieve the uniform pressure distribution on the anode surface. Further studies in using an alternative salt lithium bis(fluorosulfonyl)imide (LiFSI)-based electrolyte and full cell AFBs will also be investigated.

Conclusions

In this study, we visualized the initial lithium metal plating process on the Cu-CC surface of coin cell type AFBs. Lithium metal with a capacity of 5 mA h cm^{-2} was deposited onto the Cu-CC. Internal pressure distribution tests revealed a significant pressure distribution difference on the Cu-CC surface in coin cell type AFBs: the annual edge region experienced a pressure of 50 MPa, while the center region was subjected to 1 MPa. Using ToF-SIMS and plasma FIB-SEM imaging, we demonstrated that lithium plating on the high-pressure annular edge region exhibited large lithium grains, a dense, void-free internal structure, and a smooth, flat surface. In contrast, lithium plating on the low-pressure center region displayed small lithium grains with a loose packed, tortuous internal morphology, abundant voids, and a rough surface. The pressure distribution differences did not affect the composition of the SEI layer on the surface of lithium metal plating. However, ensuring uniform pressure distribution across the anode surface is critical for achieving homogeneous lithium metal plating in coin cell type AFBs. This study provides a unified view on the initial lithium metal plating process on a Cu-CC surface and offers a strategy for achieving a dense and favorable lithium metal microstructure in AFBs.

Author contributions

J. S. and C. H. conceived the idea for the research. C. H. supervised all aspects of the project. J. S. performed the ToF-SIMS, plasma FIB, SEM, EDX, XPS, and XRD experiments, and conducted characterization studies and electrochemical experiments. J. S and C. H. analyzed and interpreted the data and wrote the manuscript. C. H. revised the manuscript.

Conflicts of interest

There are no conflicts to declare.

Data availability

The data supporting this article have been included as part of the SI. See DOI: **https://doi.org/10.1039/d5ee01956g**

Acknowledgements

This work was supported by the Faraday Institution Degradation Project (FIRG060) and the Faraday Institution Nextrode Project (FIRG066). C. H. acknowledges funding from the ERC Starting Grant (converted to UKRI funding EP/Y009908/1), the Faraday Institution Industry Fellowship FIIF015, and the Imperial College London UKRI Impact Acceleration Account EP/X52556X/1. The authors acknowledge the cell testing equipment provided by the ATLAS project from the Department of Chemical Engineering, Imperial College London.

References

1 M. Armand and J. M. Tarascon, Building better batteries, *Nature*, 2008, **451**(7179), 652–657.
2 W. Xu, J. L. Wang, F. Ding, X. L. Chen, E. Nasybutin, Y. H. Zhang and J. G. Zhang, Lithium metal anodes for rechargeable batteries, *Energy Environ. Sci.*, 2014, **7**(2), 513–537.

3 M. Li, J. Lu, Z. W. Chen and K. Amine, 30 Years of Lithium-Ion Batteries, *Adv. Mater.*, 2018, **30**(33), 1800561.
4 Y. S. Meng, V. Srinivasan and K. Xu, Designing better electrolytes, *Science*, 2022, **378**(6624), eabq3750.
5 J. Su, T. Tsuruoka, T. Tsujita, Y. Inatomi and K. Terabe, Nitrogen Plasma Enhanced Low Temperature Atomic Layer Deposition of Magnesium Phosphorus Oxynitride (MgPON) Solid-State Electrolytes, *Angew. Chem., Int. Ed.*, 2023, **62**(9), e202217203.
6 J. W. Choi and D. Aurbach, Promise and reality of post-lithium-ion batteries with high energy densities, *Nat. Rev. Mater.*, 2016, **1**(4), 16013.
7 C. Huang, C. L. A. Leung, P. Leung and P. S. Grant, A Solid-State Battery Cathode with a Polymer Composite Electrolyte and Low Tortuosity Microstructure by Directional Freezing and Polymerization, *Adv. Energy Mater.*, 2021, **11**(1), 2002387.
8 R. Weber, M. Genovese, A. J. Louli, S. Hames, C. Martin, I. G. Hill and J. R. Dahn, Long cycle life and dendrite-free lithium morphology in anode-free lithium pouch cells enabled by a dual-salt liquid electrolyte, *Nat. Energy*, 2019, **4**(8), 683–689.
9 A. J. Louli, A. Eldesoky, R. Weber, M. Genovese, M. Coon, J. deGooyer, Z. Deng, R. T. White, J. Lee and T. Rodgers, *et al.*, Diagnosing and correcting anode-free cell failure via electrolyte and morphological analysis, *Nat. Energy*, 2020, **5**(9), 693–702.
10 J. G. Zhang, W. Xu, J. Xiao, X. Cao and J. Liu, Lithium Metal Anodes with Nonaqueous Electrolytes, *Chem. Rev.*, 2020, **120**(24), 13312–13348.
11 J. F. Qian, B. D. Adams, J. M. Zheng, W. Xu, W. A. Henderson, J. Wang, M. E. Bowden, S. C. Xu, J. Z. Hu and J. G. Zhang, Anode-Free Rechargeable Lithium Metal Batteries, *Adv. Funct. Mater.*, 2016, **26**(39), 7094–7102.
12 Z. Yu, P. E. Rudnicki, Z. W. Zhang, Z. J. Huang, H. Celik, S. T. Oyakhire, Y. L. Chen, X. Kong, S. C. Kim and X. Xiao, *et al.*, Rational solvent molecule tuning for high-performance lithium metal battery electrolytes, *Nat. Energy*, 2022, **7**(1), 94–106.
13 S. Nanda, A. Gupta and A. Manthiram, Anode-Free Full Cells: A Pathway to High-Energy Density Lithium-Metal Batteries, *Adv. Energy Mater.*, 2021, **11**(2), 2000804.
14 A. J. Louli, A. Eldesoky, J. deGooyer, M. Coon, C. P. Aiken, Z. Simunovic, M. Metzger and J. R. Dahn, Different Positive Electrodes for Anode-Free Lithium Metal Cells, *J. Electrochem. Soc.*, 2022, **169**(4), 040517.
15 J. Su, T. Hisatomi, T. Minegishi and K. Domen, Enhanced Photoelectrochemical Water Oxidation from CdTe Photoanodes Annealed with $CdCl_2$, *Angew. Chem., Int. Ed.*, 2020, **59**(33), 13800–13806.
16 C. L. A. Leung, M. D. Wilson, T. Connolley and C. Huang, Mapping of lithium ion concentrations in 3D structures through development of in situ correlative imaging of X-ray Compton scattering-computed tomography, *J. Synchrotron Radiat.*, 2024, **31**, 888–895.
17 C. Gervillié-Mouravieff, L. Ah, A. Liu, C. J. Huang and Y. S. Meng, Deciphering the Impact of the Active Lithium Reservoir in Anode-Free Pouch Cells, *ACS Energy Lett.*, 2024, **9**(4), 1693–1700.
18 A. J. Louli, M. Coon, M. Genovese, J. deGooyer, A. Eldesoky and J. R. Dahn, Optimizing Cycling Conditions for Anode-Free Lithium Metal Cells, *J. Electrochem. Soc.*, 2021, **168**(2), 020515.
19 X. B. Cheng, R. Zhang, C. Z. Zhao and Q. Zhang, Toward Safe Lithium Metal Anode in Rechargeable Batteries: A Review, *Chem. Rev.*, 2017, **117**(15), 10403–10473.
20 C. Huang, M. D. Wilson, B. Cline, A. Sivarajah, W. Stolp, M. N. Boone, T. Connolley and C. L. A. Leung, Correlating lithium-ion transport and interfacial lithium microstructure evolution in solid-state batteries during the first cycle, *Cell Rep. Phys. Sci.*, 2024, **5**(6), 101995.
21 Y. Qiao, H. J. Yang, Z. Chang, H. Deng, X. Li and H. S. Zhou, A high-energy-density and long-life initial-anode-free lithium battery enabled by a Li_2O sacrificial agent, *Nat. Energy*, 2021, **6**(6), 653–662.
22 A. B. Gunnarsdóttir, C. V. Amanchukwu, S. Menkin and C. P. Grey, Noninvasive *In Situ* NMR Study of "Dead Lithium" Formation and Lithium Corrosion in Full-Cell Lithium Metal Batteries, *J. Am. Chem. Soc.*, 2020, **142**(49), 20814–20827.
23 B. Thirnmalraj, T. T. Hagos, C. J. Huang, M. A. Teshager, J. H. Cheng, W. N. Su and B. J. Hwang, Nucleation and Growth Mechanism of Lithium Metal Electroplating, *J. Am. Chem. Soc.*, 2019, **141**(46), 18612–18623.
24 S. Kim, P. N. Didwal, J. Fiates, J. A. Dawson, R. S. Weatherup and M. De Volder, Effect of the Formation Rate on the Stability of Anode-Free Lithium Metal Batteries, *ACS Energy Lett.*, 2024, **9**(10), 4753–4760.
25 L. D. Lin, K. Qin, Q. H. Zhang, L. Gu, L. M. Suo, Y. S. Hu, H. Li, X. J. Huang and L. Q. Chen, Li- Li-Rich $Li_2Ni_{0.8}Co_{0.1}Mn_{0.1}O_2$ for Anode-Free Lithium Metal Batteries, *Angew. Chem., Int. Ed.*, 2021, **60**(15), 8289–8296.
26 S. Menkin, C. A. O'Keefe, A. B. Gunnarsdóttir, S. Dey, F. M. Pesci, Z. H. Shen, A. Aguadero and C. P. Grey, Toward an Understanding of SEI Formation and Lithium Plating on Copper in Anode-Free Batteries, *J. Phys. Chem. C*, 2021, **125**(30), 16719–16732.
27 J. Alvarado, M. A. Schroeder, T. P. Pollard, X. F. Wang, J. Z. Lee, M. H. Zhang, T. Wynn, M. Ding, O. Borodin and Y. S. Meng, *et al.*, Bisalt ether electrolytes: a pathway towards lithium metal batteries with Ni-rich cathodes, *Energy Environ. Sci.*, 2019, **12**(2), 780–794.
28 L. S. Su, H. Charalambous, Z. H. Cui and A. Manthiram, High-efficiency, anode-free lithium-metal batteries with a close-packed homogeneous lithium morphology, *Energy Environ. Sci.*, 2022, **15**, 843–854.
29 V. Pande and V. Viswanathan, Computational Screening of Current Collectors for Enabling Anode-Free Lithium Metal Batteries, *ACS Energy Lett.*, 2019, **4**(12), 2952–2959.
30 J. Su, M. Pasta, Z. Y. Ning, X. W. Gao, P. G. Bruce and C. R. M. Grovenor, Interfacial modification between argyrodite-type solid-state electrolytes and Li metal anodes using LiPON interlayers, *Energy Environ. Sci.*, 2022, **15**(9), 3805–3814.

31 Y. Zhang, J. Liu, Y. Li, D. Zhao, W. Huang, Y. Zheng, J. Zhou, C. Zhu, C. Deng, Y. Sun, T. Qian and C. Yan, Reactivating the Dead Lithium by Redox Shuttle to Promote the Efficient Utilization of Lithium for Anode Free Lithium Metal Batteries, *Adv. Funct. Mater.*, 2023, **40**, 2301332.
32 M. Peng, J. Zhou, T. Han, Y. Zhou, J. Liu, N. Xu, Z. Wang, W. Lin and C. Yan, Dynamically lithium-compensated polymer artificial SEI to assist highly stable lithium-rich manganese-based anode-free lithium metal batteries, *Rare Met.*, 2024, **43**, 2527–2535.
33 A. J. Louli, M. Genovese, R. Weber, S. G. Hames, E. R. Logan and J. R. Dahn, Exploring the Impact of Mechanical Pressure on the Performance of Anode-Free Lithium Metal Cells, *J. Electrochem. Soc.*, 2019, **166**(8), A1291–A1299.
34 C. C. Fang, B. Y. Lu, G. Pawar, M. H. Zhang, D. Y. Cheng, S. R. Chen, M. Ceja, J. M. Doux, H. Musrock and M. Cai, *et al.*, Pressure-tailored lithium deposition and dissolution in lithium metal batteries, *Nat. Energy*, 2021, **6**(10), 987–994.
35 X. Zhang, Q. J. Wang, K. L. Harrison, K. Jungjohann, B. L. Boyce, S. A. Roberts, P. M. Attia and S. J. Harris, Rethinking How External Pressure Can Suppress Dendrites in Lithium Metal Batteries, *J. Electrochem. Soc.*, 2019, **166**(15), A3639–A3652.
36 E. Kazyak, M. J. Wang, K. W. Lee, S. Yadavalli, A. J. Sanchez, M. D. Thouless, J. Sakamoto and N. P. Dasgupta, Understanding the electro-chemo-mechanics of Li plating in anode-free solid-state batteries with operando 3D microscopy, *Matter*, 2022, **5**(11), 3912–3934.
37 H. Lee, *et al.*, Electrode Edge Effects and the Failure Mechanism of Lithium-Metal Batteries, *ChemSusChem*, 2018, **11**, 3821–3828.
38 X. S. Yin, *et al.*, Insights into morphological evolution and cycling behaviour of lithium metal anode under mechanical pressure, *Nano Energy*, 2018, **50**, 659–664.
39 V. Rackwitz, M. Krumrey, C. Laubis, F. Scholze and V. D. Hodoroaba, New reference and test materials for the characterization of energy dispersive X-ray spectrometers at scanning electron microscopes, *Anal. Bioanal. Chem.*, 2015, **407**(11), 3045–3053.
40 Y. H. Zhao, S. K. Otto, T. Lombardo, A. Henss, A. Koeppe, M. Selzer, J. Janek and B. Nestler, Identification of Lithium Compounds on Surfaces of Lithium Metal Anode with Machine-Learning-Assisted Analysis of ToF-SIMS Spectra, *ACS Appl. Mater. Interfaces*, 2023, **15**(43), 50469–50478.
41 J. C. Stallard, S. Vema, C. P. Grey, V. S. Deshpande and N. A. Fleck, The strength of a constrained lithium layer, *Acta Mater.*, 2023, **260**, 119313.

